Pulsed EM field, close-range signal transfer in layered configurations - A time-domain analysis

Lager, IE; Voogt, V; Kooij, BJ

DOI
10.1109/TAP.2014.2307588

Publication date
2014

Document Version
Accepted author manuscript

Published in
IEEE Transactions on Antennas and Propagation

Pulsed EM Field, Close-Range Signal Transfer in Layered Configurations—A Time-Domain Analysis

Ioan E. Lager, *Senior Member, IEEE*, Vincent Voogt, and Bert Jan Kooij

***Abstract*—The pulsed electromagnetic (EM)-field propagation in configurations that are of relevance for the radiation from integrated antennas is examined. The investigated configurations consist of layered structures with material parameters that are typical for integrated circuits fabricated in complementary metal–oxide semiconductor technology, and are excited via small, conducting, current-carrying loops. Space-time expressions of the EM-field quantities are derived by using the modified Cagniard method. After validating it by means of comparisons with analytical results, the devised framework is used for examining the radiated field in the proximity of a chip. This study is instrumental for the analysis and design of close-range digital signal transfer.**

***Index Terms*—Electromagnetic radiation, time-domain analysis.**

I. Introduction

THE EXPLOSIVE digital data exchange in nomadic applications is the driving force behind ever faster wireless data transfer, with rates of 10 Gb/s (or higher) being deemed possible [1]. Offering such performance, while conforming to the international spectrum regulations, pushes the capacity of the radio channel to its physical limits.

Due to its intrinsically localized, low-power operation, the close-range, interchip, digital signal transfer constitutes a class of wireless applications that optimally make use of the radio channel's physical capacity, while precluding collision with spectrum regulations. These applications are most opportunely implemented by means of *the pulsed electromagnetic (EM)-field signal transfer*. This approach is, moreover, requisite to situations requiring a combination of communication, localization, and imaging [2].

The feasibility of the (close-range) pulsed EM field, wireless transfer was demonstrated in [3] for a basic, yet illustrative, interchip digital communication setup. A more realistic configuration, accounting for the typical (layered) structure in integrated circuits (ICs), was preliminarily examined in [4]. The relevant space-time Green's functions were obtained via the modified Cagniard method (the "Cagniard-DeHoop method") [5]–[7], a mathematical instrument with increasingly wider use in ultrawideband (UWB) antenna studies [8], [9].

This paper presents for the first time a detailed, *time-domain* (TD) analysis of the EM field radiated by an integrated loop antenna, as habitually realized in (Bi)complementary metal–oxide semiconductor (CMOS) technology. The framework bares some similarity with approaches in the widely investigated class of *frequency-domain* formulations for the analysis of layered structures [10]–[23]. However, by employing a causality preserving formulation, the avenue chosen in this paper offers definite conceptual advantages for the study of *digital* wireless transfer that involves pulsed, as opposed to time-harmonic, signals. The proposed methodology is, moreover, highly versatile, being suitable for studying various (model) layered configurations. Nonetheless, for maintaining the focus on the close-range wireless transfer, its formulation is tailored in this paper to the analysis of the free-space EM-field propagation in the near-field region, with aspects such as the far-field, free space radiation (as required by electromagnetic compatibility studies), or the in-slab, guided propagation (as required by crosstalk estimation) being left deliberately outside the scope of the analysis.

In the following sections, a realistic model configuration is first devised. Expressions of the space-time, EM-field quantities in the free space outside the integrated circuit (IC) are subsequently derived, with technical details being elaborately explained in the Appendices. The obtained formulation is first validated against analytic results concerning the field radiated by a small, conducting, current-carrying loop in free space, and is subsequently employed for examining the EM radiation of a CMOS integrated-loop antenna. Conclusions round off the account.

II. Model Configuration

The model configuration employed in this study mimicks a CMOS integrated (loop) antenna fabricated via the process described in [24]. The relevant antenna is sandwiched between a very low conductivity SiO_2 layer and an insulating passivation layer with matched permittivity. This compound is deposited on top of a conductive Si substrate. In a first approximation, SiO_2 can be taken as an insulator; this allows coalescing the oxide and passivation layers into one slab, with the antenna being immersed parallel to the slab's faces. Furthermore, the losses in the substrate are sufficiently high to completely damp out any reflection from interfaces underneath it.

Based on this, the configuration in Fig. 1 (baring similitude with the one in [25]) is devised. With reference to a

Manuscript received July 18, 2013; revised February 04, 2014; accepted February 11, 2014. Date of publication February 21, 2014; date of current version May 01, 2014.

The authors are with the Faculty of Electrical Engineering, Mathematics and Computer Science, Delft University of Technology, Delft 2628 CD, the Netherlands (e-mail: i.e.lager@tudelft.nl; v.voogt@student.tudelft.nl; b.j.kooij@tudelft.nl).

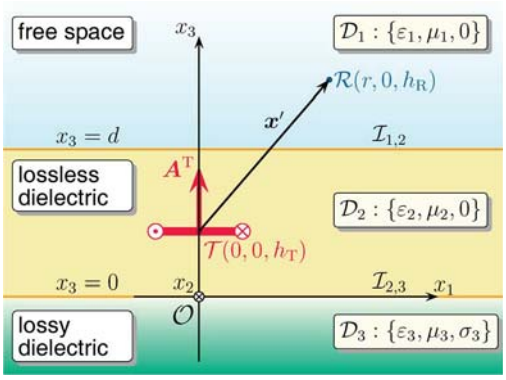

Fig. 1. Model configuration concerning the pulsed EM field radiated by a transmitting wire loop in a three media layered structure.

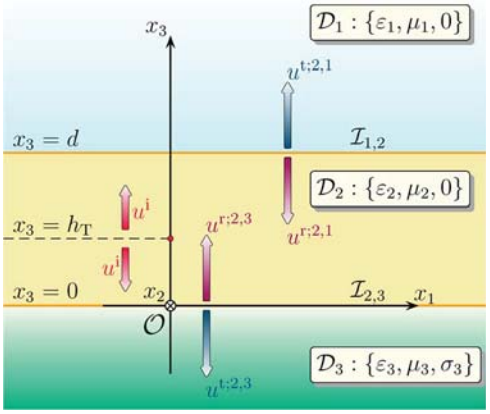

Fig. 2. Explicative for the waves in the model configuration in Fig. 1.

TABLE I
ELECTROMAGNETIC PROPERTIES OF THE MEDIA IN THE MODEL CONFIGURATION

Domain	Relative permittivity ε_r	Relative permeability μ_r	Conductivity σ (Sm^{-1})
$\mathcal{D}_1$	1	1	0
$\mathcal{D}_2$	3.9	1	0
$\mathcal{D}_3$	11.7	1	10^{-3}

right-handed, orthogonal Cartesian frame with coordinates $\{x_1, x_2, x_3\}$, the model consists of a conductive substrate $\mathcal{D}_3 = \{-\infty < x_{1,2} < \infty, x_3 < 0\}$; an insulating (dielectric) slab $\mathcal{D}_2 = \{-\infty < x_{1,2} < \infty, 0 < x_3 < d\}$, $d > 0$; and free space $\mathcal{D}_1 = \{-\infty < x_{1,2} < \infty, d < x_3\}$. The values of the electric permittivity ε, magnetic permeability μ, and conductivity σ are given in Table I, and the material parameters for Si and the compound SiO_2/passivation slab are chosen based on [26]. The wave speeds in $\mathcal{D}_i$, $i = 1, 2, 3$, are $c_i = (\varepsilon_i \mu_i)^{-1/2}$. A transmitting wire loop, of vanishing wire diameter and vectorial area $\boldsymbol{A}^\mathrm{T} = A^\mathrm{T} \boldsymbol{i}_3$, is located in $\mathcal{D}_2$. Without loss of generality, its reference center $\mathcal{T}$ is taken at $\boldsymbol{x}^\mathrm{T} = h_\mathrm{T} \boldsymbol{i}_3$, $0 < h_\mathrm{T} < d$. The loop is electrically small with respect to the pulse's spatial extent $c_2 t_\mathrm{w}$, with t_w being the (conventional) pulsewidth, and is fed at its Kirchhoff port by a pulsed electric current $I^\mathrm{T}(t)$, with t denoting the time coordinate. This analysis is confined to determining EM-field quantities in $\mathcal{D}_1$. The observation point is then taken at $\boldsymbol{x}^\mathrm{R} = x_1 \boldsymbol{i}_1 + x_2 \boldsymbol{i}_2 + h_\mathrm{R} \boldsymbol{i}_3$, with $h_\mathrm{R} > d$ and, correspondingly, the relative position vector is $\boldsymbol{x}' = \boldsymbol{x} - \boldsymbol{x}^\mathrm{T}$.

Hereafter, ∂_m, $m = 1, 2, 3$, denotes partial differentiation with respect to x_m, and ∂_t denotes partial differentiation with respect to t.

III. SPACE-TIME EXPRESSIONS OF THE EM-FIELD QUANTITIES IN FREE SPACE

The expressions of the EM-field quantities, that is, the electric $\boldsymbol{E}(\boldsymbol{x}', t)$ and magnetic $\boldsymbol{H}(\boldsymbol{x}', t)$ field strengths, are now derived. Only the steps that are essential for understanding the formulation will be presented, with details concerning the discussed framework being available in [27].

A. Field Quantities

Since the transmit loop antenna is electrically small, it is assimilated to a *vertical magnetic dipole* located at its reference center. In line with [28], [29, Sec. 2.2.2], the TE-polarized EM field radiated by the magnetic dipole is expressed inside each subdomain of continuity $\mathcal{D}_i$, $i = 1, 2, 3$, as

$$\boldsymbol{E}(\boldsymbol{x}', t) = -\mu \left(\boldsymbol{i}_1 \partial_2 - \boldsymbol{i}_2 \partial_1\right) \partial_t u(\boldsymbol{x}', t) \tag{1}$$

$$\boldsymbol{H}(\boldsymbol{x}', t) = \boldsymbol{\nabla} \left[\partial_3 u(\boldsymbol{x}', t)\right] - \boldsymbol{i}_3 \mu \varepsilon \partial_t^2 u(\boldsymbol{x}', t) - \boldsymbol{i}_3 \mu \sigma \partial_t u(\boldsymbol{x}', t) \tag{2}$$

with the potential function u $(\mathrm{m} \cdot \mathrm{A})$ satisfying the dissipative wave equation[1]

$$\boldsymbol{\nabla}^2 u - c_i^{-2} \partial_t^2 u - \sigma_i \mu_i \partial_t u = 0, \quad \text{for } i = 1, 2, 3. \tag{3}$$

With reference to Fig. 2, three types of waves are distinguished: 1) *incident waves*, denoted by the superscript "i," that is, the ones propagating away from the source and not interacting with any of the interfaces; 2) *reflected waves*, denoted by the superscript "r," that is, the ones reflected at interfaces; 3) *transmitted waves*, denoted by the superscript "t," that is, the ones transmitted through interfaces. The relevant superscripts are complemented for the reflected and transmitted waves by the corresponding interface identifier. Note that since $\mathcal{D}_1$ and $\mathcal{D}_3$ are semi-infinite half-spaces, no reflected waves exist in them. With these notations, the potential function is given by

$$u = \begin{cases} u^{\mathrm{t};2,1}, & \text{for } \infty < x_3' < d \\ (u^\mathrm{i} + u^{\mathrm{r};2,1} + u^{\mathrm{r};2,3}), & \text{for } d < x_3' < 0 \\ u^{\mathrm{t};2,3}, & \text{for } 0 < x_3' < -\infty. \end{cases} \tag{4}$$

The incident potential functions (with support in $\mathcal{D}_2$) are [4]

$$u^\mathrm{i} = \frac{m\left(t - |\boldsymbol{x}'|/c_2\right)}{4\pi |\boldsymbol{x}'|} \tag{5}$$

where $m = A^\mathrm{T} I^\mathrm{T}(t)$ $(\mathrm{m}^2 \cdot \mathrm{A})$ is the magnetic moment. The other potential functions in (4) follow from u^i by accounting for the relevant reflection and transmission coefficients.

[1]For brevity, the explicit statement of the $\boldsymbol{x}'$ and t dependence is henceforth dropped.

B. Boundary Conditions

For guaranteeing the standard interface boundary conditions applying to $\boldsymbol{E}$ and $\boldsymbol{H}$, the following interface boundary conditions are enforced at $\mathcal{I}_{1,2}$ and $\mathcal{I}_{2,3}$ [28]:

$$\lim_{x_3\downarrow 0}(\partial_3 u^{\mathrm{i}} + \partial_3 u^{\mathrm{r};2,1} + \partial_3 u^{\mathrm{r};2,3}) = \lim_{x_3\uparrow 0} \partial_3 u^{\mathrm{t};2,3} \quad (6)$$

$$\lim_{x_3\downarrow 0}(u^{\mathrm{i}} + u^{\mathrm{r};2,1} + u^{\mathrm{r};2,3}) = \lim_{x_3\uparrow 0} u^{\mathrm{t};2,3} \quad (7)$$

$$\lim_{x_3\uparrow d}(\partial_3 u^{\mathrm{i}} + \partial_3 u^{\mathrm{r};2,1} + \partial_3 u^{\mathrm{r};2,3}) = \lim_{x_3\downarrow d} \partial_3 u^{\mathrm{t};2,1} \quad (8)$$

$$\lim_{x_3\uparrow d}(u^{\mathrm{inc}} + u^{\mathrm{r};2,1} + u^{\mathrm{r};2,3}) = \lim_{x_3\downarrow d} u^{\mathrm{t};2,1}. \quad (9)$$

C. Spectral Domain Representations

Equations (1)–(9) are now subjected to a Laplace transform with respect to the time coordinate t, followed by an s-scaled Fourier transform with respect to the space coordinates x_1 and x_2. The Laplace transform of an arbitrary, *causal* function $f(\boldsymbol{x}, t)$ is given by[2]

$$\hat{f}(\boldsymbol{x}, s) = \int_{t=0}^{\infty} f(\boldsymbol{x}, t)\exp(-st)\mathrm{d}t, \quad \text{for } s \in \mathbb{R}, \quad s > 0 \quad (10)$$

where the choice for $s \in \mathbb{R}$, $s > 0$ is requisite, via Lerch's theorem [30], [31, Sec. II.6] for ensuring the uniqueness of the inverse transformation. The scaled Fourier transform is given by

$$\tilde{f}(\alpha_1, \alpha_2, x_3, s) = \int_{x_1=-\infty}^{\infty}\int_{x_1=-\infty}^{\infty} \hat{f}(x_1, x_2, x_3, s) \times \exp\left[s(\alpha_1 x_1 + \alpha_2 x_2)\right]\mathrm{d}x_1\mathrm{d}x_2 \quad (11)$$

with $s\alpha_1, s\alpha_2 \in \mathbb{C}$, $\mathrm{Re}(s\alpha_1) = \mathrm{Re}(s\alpha_2) = 0$. Note that the aforementioned choice for s is again beneficial, allowing to select conveniently $\alpha_1 = \mathrm{i}z'$, $\alpha_2 = \mathrm{i}z''$, $z', z'' \in \mathbb{R}$. The inverse scaled Fourier transform then follows as:

$$\hat{f}(\boldsymbol{x}, s) = \left(\frac{s}{2\pi\mathrm{i}}\right)^2 \int_{\alpha_2=-\mathrm{i}\infty}^{\mathrm{i}\infty}\int_{\alpha_1=-\mathrm{i}\infty}^{\mathrm{i}\infty} \tilde{f}(\alpha_1, \alpha_2, x_3, s) \times \exp\left[-s(\alpha_1 x_1 + \alpha_2 x_2)\right]\mathrm{d}\alpha_1\mathrm{d}\alpha_2. \quad (12)$$

By applying the spectral domain transformations in (10) and (11), (3) results in

$$\partial_3^2\tilde{u} - s^2\left[\gamma_i^2 + s^{-1}\mu_i\sigma_i\right]\tilde{u} = 0, \quad \text{for } i = 1, 2, 3. \quad (13)$$

with the propagation coefficient γ being

$$\gamma_i(\alpha_1, \alpha_2) = \left[c_i^{-2} - \left(\alpha_1^2 + \alpha_2^2\right)\right]^{\frac{1}{2}}, \quad \text{with } \mathrm{Re}(\gamma_i) \geqslant 0, \quad \text{for } i = 1, 2, 3. \quad (14)$$

[2]Since all physical quantities dealt with in this paper have bounded values, the condition $\mathrm{Re}(s) > 0$ suffices for ensuring the absolute convergence of the Laplace integral.

As stated in Section II, the analysis is restricted to observation points in $\mathcal{D}_1$. Consequently, solving (13) and applying the spectral domain transformed relations (5)–(9) yields

$$\tilde{u}^{\mathrm{t};2,1} = \sum_{n=0}^{\infty}\Bigg(\frac{\hat{m}(s)}{2s\gamma_2}T_{2,1} \times \Big\{R_{2,1}^n\hat{R}_{2,3}^n\exp\left[-s(\gamma_1 Z_1 + \gamma_2 Z_{\uparrow;2})\right] + R_{2,1}^n\hat{R}_{2,3}^{n+1}\exp\left[-s(\gamma_1 Z_1 + \gamma_2 Z_{\downarrow;2})\right]\Big\}\Bigg) \quad (15)$$

where n is a counter for the *double* reflections at the interfaces $\mathcal{I}_{1,2}$ and $\mathcal{I}_{2,3}$, $\hat{m}(s)$ is the Laplace transform of $m(t)$, $T_{2,1}$ is the transmission coefficient at $\mathcal{I}_{1,2}$

$$T_{2,1} = 1 + R_{2,1} \quad (16)$$

with

$$R_{2,1} = \frac{\gamma_2 - \gamma_1}{\gamma_2 + \gamma_1} \quad (17)$$

being the reflection coefficient at $\mathcal{I}_{1,2}$.

$$\hat{R}_{2,3}(s) = \frac{\gamma_2 - \left(\gamma_3^2 + s^{-1}\sigma_3\mu_3\right)^{\frac{1}{2}}}{\gamma_2 + \left(\gamma_3^2 + s^{-1}\sigma_3\mu_3\right)^{\frac{1}{2}}}, \quad \text{with } \mathrm{Re}\left[\left(\gamma_3^2 + s^{-1}\sigma_3\mu_3\right)^{\frac{1}{2}}\right] \geqslant 0 \quad (18)$$

is the reflection coefficient at $\mathcal{I}_{2,3}$ and

$$Z_1 = x_3 - d \quad (19)$$

$$Z_{\uparrow;2} = (2n+1)d - h_{\mathrm{T}} \quad (20)$$

$$Z_{\downarrow;2} = (2n+1)d + h_{\mathrm{T}}. \quad (21)$$

From (15), it can be readily inferred that $\tilde{u}^{\mathrm{t};2,1}$ is obtained as an infinite superposition of two types of "generalized rays" [9], namely "rays" that originate from incident waves propagating upward and downward (in the $\boldsymbol{i}_3$ and $-\boldsymbol{i}_3$ directions, respectively), and their multiple reflections at the interfaces. Note that there is one "ray" originating from the upward incident wave that does not undergo any reflection.

Substitution of (15) into the spectral domain counterparts of (1) and (2) yields the spectral domain field quantities

$$\tilde{E}_1^{\mathrm{t};2,1}(\alpha_1, \alpha_2, x_3, s) = \mu_1 s^2\alpha_2\tilde{u}^{\mathrm{t};2,1} \quad (22)$$

$$\tilde{E}_2^{\mathrm{t};2,1}(\alpha_1, \alpha_2, x_3, s) = -\mu_1 s^2\alpha_1\tilde{u}^{\mathrm{t};2,1} \quad (23)$$

$$\tilde{E}_3^{\mathrm{t};2,1}(\alpha_1, \alpha_2, x_3, s) = 0 \quad (24)$$

$$\tilde{H}_1^{\mathrm{t};2,1}(\alpha_1, \alpha_2, x_3, s) = s^2\alpha_1\gamma_1\tilde{u}^{\mathrm{t};2,1} \quad (25)$$

$$\tilde{H}_2^{\mathrm{t};2,1}(\alpha_1, \alpha_2, x_3, s) = s^2\alpha_2\gamma_1\tilde{u}^{\mathrm{t};2,1} \quad (26)$$

$$\tilde{H}_3^{\mathrm{t};2,1}(\alpha_1, \alpha_2, x_3, s) = s^2\left(\gamma_1^2 - \mu_1\varepsilon_1\right)\tilde{u}^{\mathrm{t};2,1}. \quad (27)$$

By applying the inverse Fourier transform (12) to (22)–(27), the relevant components are expressed generically as

$$\hat{w}_k^{E,H}(\boldsymbol{x}',s)=s^3\hat{m}(s)\sum_{\varsigma=\uparrow,\downarrow}\sum_{n=0}^{\infty}\hat{g}_{k;\varsigma;n}^{E,H}(\boldsymbol{x}',s),\ \text{for } k=1,2,3 \tag{28}$$

where the combination of superscripts E, H and indices $k = 1, 2, 3$ refers to the relevant EM-field quantity components and $\hat{g}_{k;\varsigma;n}^{E,H}$ represents the corresponding Green's functions[3]

$$\hat{g}_{k;\varsigma;n}^{E,H}(\boldsymbol{x}',s)=\frac{-1}{8\pi^2}\int_{\alpha_2=-\mathrm{i}\infty}^{\mathrm{i}\infty}\int_{\alpha_1=-\mathrm{i}\infty}^{\mathrm{i}\infty}\hat{G}_{k;\varsigma;n}^{E,H}(\alpha_1,\alpha_2,s)\times\exp\left[-s(\alpha_1x_1+\alpha_2x_2+\gamma_1Z_1+\gamma_2Z_{\varsigma;2})\right]\mathrm{d}\alpha_2\mathrm{d}\alpha_1 \tag{29}$$

with $\hat{G}_{k;\varsigma;n}^{E,H}$ being the *ray functions* (s/m)

$$\hat{G}_{k;\uparrow;n}^{E,H}(\alpha_1,\alpha_2,s)=\frac{T_{2,1}R_{2,1}^n\hat{R}_{2,3}^n(s)}{\gamma_2} \tag{30}$$

$$\hat{G}_{k;\downarrow;n}^{E,H}(\alpha_1,\alpha_2,s)=\frac{T_{2,1}R_{2,1}^n\hat{R}_{2,3}^{n+1}(s)}{\gamma_2} \tag{31}$$

for $k = 1, 2, 3$ and $n = 0, 1, 2, \ldots$.

D. Time-Domain EM-Field Quantities

The Cagniard–DeHoop method [5]–[7] is now applied for the inverse transformation to the time domain. To this end, a change of variables $\{\alpha_1,\alpha_2\}\mapsto\{\omega,q\}$, with $\omega\in\mathbb{C}$, $q\in\mathbb{R}$

$$\alpha_1=\omega\cos(\varphi)-\mathrm{i}q\sin(\varphi) \tag{32}$$

$$\alpha_2=\omega\sin(\varphi)+\mathrm{i}q\cos(\varphi) \tag{33}$$

is first applied in (29), $\{r,\varphi\}$ following from $\{x_1,x_2\}$ via polar mapping. The substitution of (32) and (33) in (14) yields

$$\gamma_i(\omega,q)=\left[\Omega_i^2-\omega^2\right]^{\frac{1}{2}},\quad\text{with }\mathrm{Re}(\gamma_i)\geqslant 0,\quad\text{for } i=1,2,3 \tag{34}$$

where

$$\Omega_i=\left[c_i^{-2}+q^2\right]^{\frac{1}{2}},\quad\text{for } i=1,2,3. \tag{35}$$

Note that γ_i does not depend on φ. Furthermore, (27) does also not depend on φ; this is consistent with the required rotational symmetry of H_3. By now using the change of variables $\{\alpha_1,\alpha_2\}\mapsto\{\omega,q\}$ in (29), it is found that

$$\hat{g}_{k;\varsigma;n}^{E,H}(\boldsymbol{x}',s)=\frac{-1}{8\pi^2}\int_{q=-\infty}^{\infty}\int_{\omega=-\mathrm{i}\infty}^{\mathrm{i}\infty}\mathrm{i}\hat{G}_{k;\varsigma;n}^{E,H}(\omega,q,s)\times\exp\left[-s(\omega r+\gamma_1Z_1+\gamma_2Z_{\varsigma;2})\right]\mathrm{d}\omega\mathrm{d}q \tag{36}$$

that contains one single integral along the imaginary axis.

The next step in the Cagniard–DeHoop method is deforming the integration path for the ω-integral to a suitably chosen contour, the goal being to derive an expression from which the inverse Laplace transform can be inferred by inspection. This procedure requires the ray functions to be independent of s. However, from (18), (30), and (31) it is clear that $\hat{R}_{2,3}$ does depend on s due to the nonzero conductivity in $\mathcal{D}_3$.

For handling the s-dependence, $\hat{R}_{2,3}^n(s)$ is rewritten as

$$\hat{R}_{2,3}^n(s)=R_{0;n}+\int_{\kappa=0}^{\infty}R_{\mathrm{D};n}(\kappa)\exp(-s\kappa)\mathrm{d}\kappa,\ \text{for } n=0,1,2,\ldots \tag{37}$$

where

$$R_{0;n}=\lim_{|s|\to\infty}\hat{R}_{2,3}^n(s)=\left(\frac{\gamma_2-\gamma_3}{\gamma_2+\gamma_3}\right)^n \tag{38}$$

is the instantaneous response of the reflection coefficient (an s-independent quantity) and

$$R_{\mathrm{D};n}(\kappa)=\frac{1}{2\pi\mathrm{i}}\int_{p\in\mathrm{Br}}\hat{R}_{\mathrm{D};n}(p)\exp(p\kappa)\mathrm{d}p,\quad\text{for }\mathrm{Re}(p)>0 \tag{39}$$

with Br denoting the Bromwich path and $\hat{R}_{\mathrm{D};n}(p)=\hat{R}_{2,3}^n(p)-R_{0;n}$. The κ variable in (37) can be interpreted as a time relaxation due to the losses in $\mathcal{D}_3$. By using the procedure described in Appendix B, $R_{\mathrm{D};n}(\kappa)$ is expressed as

$$R_{\mathrm{D};n}(\kappa)=\frac{\beta\mathrm{i}}{4\pi}\int_{\psi=0}^{2\pi}\left\{\frac{\gamma_2\left[1-\cos(\psi)\right]+\mathrm{i}\gamma_3\sin(\psi)}{\gamma_2\left[1-\cos(\psi)\right]-\mathrm{i}\gamma_3\sin(\psi)}\right\}^n\times\exp\left\{-\beta/2\left[1-\cos(\psi)\right]\kappa\right\}\sin(\psi)\mathrm{d}\psi \tag{40}$$

with β being introduced in (58), that transforms (36) into

$$\hat{g}_{k;\varsigma;n}^{E,H}(\boldsymbol{x}',s)=\frac{-1}{8\pi^2}\int_{q=-\infty}^{\infty}\int_{\omega=-\mathrm{i}\infty}^{\mathrm{i}\infty}\int_{\kappa=0}^{\infty}\mathrm{i}G_{k;\varsigma;n}^{E,H}(\omega,q)\times\exp\left[-s(\omega r+\gamma_1Z_1+\gamma_2Z_{\varsigma;2}+\kappa)\right]\mathrm{d}\kappa\mathrm{d}\omega\mathrm{d}q \tag{41}$$

where

$$G_{k;\varsigma;n}^{E,H}=\int_{\kappa=0}^{\infty}\frac{T_{2,1}R_{2,1}^n}{\gamma_2}\left[R_{0;n_\varsigma}\delta(\kappa)+R_{\mathrm{D};n_\varsigma}\delta(\kappa)\right]\mathrm{d}\kappa \tag{42}$$

with $n_\varsigma = n$ or $n+1$ for $\varsigma=\uparrow$ or $\downarrow$, respectively, and $\delta(\cdot)$ is the Dirac delta distribution. Note that $G_{k;\varsigma;n}^{E,H}$ is an s independent quantity.

To recognize a Laplace transform in (41), the following parametrization is introduced:

$$\xi(q,\omega)=\omega r+\gamma_1Z_1+\gamma_2Z_{\varsigma;2},\quad\text{with }\xi\in\mathbb{R} \tag{43}$$

that deforms the integration path for the ω-integral into the "Cagniard-DeHoop" contour $\mathcal{C}-\mathcal{H}=\omega(\xi)\cup\omega^*(\xi)$, with ω_0 being its intersection with the real ω axis (see Appendix A for details). Equation (43) induces a mapping $T(q)=\xi(q,\omega_0)$ with $q=Q(\xi)$ as its inverse. Furthermore, let

$$\tau(q,\omega,\kappa)=\xi(q,\omega)+\kappa,\ \text{with }\tau\in\mathbb{R}\text{ and }0<\tau_\mathrm{a}\leqslant\tau. \tag{44}$$

[3]From (24), it is evident that $\hat{g}_{3,\varsigma;n}^{E}=0$. This condition will be hereafter implicitly accounted for.

The *real* parameter τ is the time coordinate consisting of two distinct *real* constituents, that is, ξ that corresponds to the standard application of the Cagniard–DeHoop method—the lossless time parameter, and the time relaxation κ that was introduced in (37). Accordingly, $\tau_{\mathrm{a}} = \tau(0, \omega_0, 0)$ is assimilated to the ray's arrival time at the observation point. Note that (43) implies that $q = Q(\tau)|_{\kappa=0}$. With these prerequisites, the procedure discussed in Appendix C yields

$$\hat{g}^{E,H}_{k;\varsigma;n}(\boldsymbol{x}', s) = \frac{1}{4\pi^2} \int_{\tau=\tau_{\mathrm{a}}}^{\infty} \exp(-s\tau)\mathrm{d}\tau \int_{q=-Q(\tau)}^{Q(\tau)} \int_{\xi=T(q)}^{\tau} \times \mathrm{Im}\left\{ \frac{G^{E,H}_{k;\varsigma;n}\left[\omega(\xi), q\right]}{\left(r - \omega\gamma_1^{-1} Z_1 - \omega\gamma_2^{-1} Z_{\varsigma;2}\right)} \right\} \mathrm{d}\xi\mathrm{d}q. \quad (45)$$

At this point, the Green's functions can be transformed back to the time domain by inspection as

$$g^{E,H}_{k;\varsigma;n}(\boldsymbol{x}', \tau) = \frac{H(t-\tau_a)}{4\pi^2} \times \int_{q=-Q(\tau)}^{Q(\tau)} \int_{\xi=T(q)}^{\tau} \mathrm{Im}\left\{ \frac{G^{E,H}_{k;\varsigma;n}\left[\omega(\xi), q\right]}{\left(r - \omega\gamma_1^{-1} Z_1 - \omega\gamma_2^{-1} Z_{\varsigma;2}\right)} \right\} \mathrm{d}\xi\mathrm{d}q \quad (46)$$

with $H(\cdot)$ denoting the Heaviside step function. Finally, the space-time expressions of the EM-field quantities are obtained by accounting for the inverse Laplace transform in (28) as

$$w^{E,H}_{k}(\boldsymbol{x}', t) = \int_{\tau=\tau_{\mathrm{a}}}^{t} \partial^3_{t-\tau} m(t-\tau) \sum_{\varsigma=\uparrow,\downarrow} \sum_{n=0}^{\infty} g^{E,H}_{k;\varsigma;n}(\boldsymbol{x}', \tau)\mathrm{d}\tau, \quad \text{for } k = 1, 2, 3. \quad (47)$$

Once the expressions of the free-space-radiated EM-field quantities were established, the received equivalent Thévenin circuit generator voltage can be derived by using the methodology developed in [32].

IV. Illustrative Numerical Experiments

The formulation derived at Section III was implemented in a Matlab code.

After discussing some basic software implementation choices, the code will be first validated by using the analytic expressions of the EM field radiated by a small, conducting, current-carrying loop in free space (see [33, Sec. 26.9 and 26.10] and [34]) and then employed for examining the model configuration in Fig. 1. This section is concluded by stressing the computational and conceptual advantages yielded by the EM-field analysis framework advocated in this paper.

A. Implementation Aspects

1) Spatial Sampling: In view of the configuration's rotational symmetry, the EM-field quantities are evaluated at $\boldsymbol{x}^{\mathrm{R}} = x_1\boldsymbol{i}_1 + h_{\mathrm{R}}\boldsymbol{i}_3$, with $x_1 > 0$. This case is representative for arbitrary observation points.

2) Excitation: The exciting electric current $I^{\mathrm{T}}(t)$ is taken as the time derivative of the unipolar, power-exponential (PE) pulse [35]

$$I^{\mathrm{T}}(t) = I_{\mathrm{peak}} N(\nu) \left(1 - \frac{t}{t_{0\mathrm{x}}}\right) \left(\frac{t}{t_{0\mathrm{x}}}\right)^{\nu-1} \times \exp\left[-\nu\left(\frac{t}{t_{0\mathrm{x}}} - 1\right)\right] H(t) \text{ for } \nu > 1 \quad (48)$$

where I_{peak} is the first peak magnitude in $I^{\mathrm{T}}(t)$, $t_{0\mathrm{x}}$ is the pulse zero-crossing time (corresponding to the pulse rise time of the PE pulse), ν is the initial rise power of the PE pulse (which is related to the high-frequency asymptotic falloff in its Bode plot), and $N(\nu)$ is the normalization constant

$$N(\nu) = \nu^{\frac{1}{2}} \left(\frac{\nu^{\frac{1}{2}}}{\nu^{\frac{1}{2}} - 1}\right)^{\nu-1} \exp\left(-\nu^{\frac{1}{2}}\right). \quad (49)$$

In all experiments, ν is taken to be an integer and larger than 4. This prevents any jump discontinuity at the pulse's onset in the time derivatives intervening in the field expressions. The (conventional) pulsewidth t_{w} follows from equating:

$$I^2_{\mathrm{peak}} t_{\mathrm{w}} = \int_{t=0}^{\infty} I^{\mathrm{T}^2}(t)\mathrm{d}t \quad (50)$$

that results into

$$t_{\mathrm{w}} = t_{0\mathrm{x}} \left[\nu N \exp(\nu)\right]^2 \frac{\Gamma(2\nu - 1)}{2\nu^{2\nu}} \quad (51)$$

where $\Gamma(\cdot)$ denotes the Euler gamma function. The chosen feeding pulse carries no net electric charge. The time Laplace transform of (48) is

$$\hat{I}^{\mathrm{T}}(s) = I_{\mathrm{peak}} t_{0\mathrm{x}} N(\nu) \frac{s t_{0\mathrm{x}} \Gamma(\nu) \exp(\nu)}{(s t_{0\mathrm{x}} + \nu)^{\nu+1}} \text{ with } \mathrm{Re}(s) > -\nu/t_{0\mathrm{x}}. \quad (52)$$

The numerical experiments are carried out for a transmitting loop with $A^{\mathrm{T}} = 0.0314\ \mathrm{mm}^2$ (for circular loops, this amounts to a diameter of 0.2 mm, a dimension that is consistent with the devices studied in [36]). The pulse is taken to have the parameters $\nu = 5$ and $t_{0\mathrm{x}} = 0.1$ ns, the latter yielding via (51) a pulse spatial extent $c_2 t_{\mathrm{w}} \approx$9 mm that concurs with the radiator being electrically small.

3) Computation of the EM-Field Quantities: With reference to (44), (46), and (47), the following elements are essential for the computation of the EM-field quantities:

- determining $\mathcal{C} - \mathcal{H}$, the relevant points follow from solving a quadratic equation;
- evaluating an integral over q, the integration limits are obtained via the mapping $q = Q(\tau)$;
- evaluating an integral over ξ, the lower integration limits are obtained via the mapping $\xi = T(q)$;
- determining the arrival times τ_{a};
- evaluating a convolution integral.

The integrals over q use either an adaptive integration scheme (the `quadl` Matlab function) or the trapezoidal rule (the `trapz` Matlab function). Note that coordinate stretching is employed

for circumventing the singularity of the integrand in (47). All equations, including the ones needed for constructing the mappings, are solved numerically.

The convolution integrals are implemented using the trapezoidal rule. For minimizing the computational effort, $g^{E,H}_{k;\varsigma;n}(\boldsymbol{x}',\tau)$ is oversampled by means of the `interp` Matlab function (using the interpolation scheme in [37, Sec. 8.1]). By denoting $\Delta t_{\rm conv}$ as the relevant time integration step, this strategy allowed sampling $g^{E,H}_{k;\varsigma;n}(\boldsymbol{x}',\tau)$ at intervals up to $20\Delta t_{\rm conv}$ without significant loss of accuracy in the integrals' evaluation when compared with $\Delta t_{\rm conv}$ sampling. More implementation details can be found in [27, Ch. 7].

B. EM Field Radiated by a Small, Conducting, Current-Carrying Loop in Free Space

The first experiment concerns a comparison of the results evaluated by means of the present method for $\varepsilon_1 = \varepsilon_2 = \varepsilon_0$, with the corresponding values following from the analytic expressions for the EM field radiated by a small, conducting, current-carrying loop in free space. The "direct ray," that is, the one corresponding to $\varsigma = \uparrow$ and $n = 0$, is accounted for, exclusively, this being equivalent to removing the reflections from the lower half-space. In the plots, the field quantities are normalized with respect to $|E_2^{\rm av}|_{\max} = \max[|E_2^{\rm av}(\boldsymbol{x}',t)|]$ and $|\boldsymbol{H}^{\rm av}|_{\max} = \max[|\boldsymbol{H}^{\rm av}(\boldsymbol{x}',t)|]$, with the superscript "av" designating "analytical values." Furthermore, the normalized arrival time retarded, time coordinate $(t-\tau_{\rm a})/t_{0\rm x}$, with $\tau_{\rm a} = |\boldsymbol{x}'|/c_1$ is employed.

The results corresponding to $\boldsymbol{x}' = 4\boldsymbol{i}_1 + 1\boldsymbol{i}_3\ (\rm mm)$ are shown in Fig. 3. From the plots, it is evident that the discussed method accurately replicates the analytic results. An extremely reduced deviation manifests itself at late times as a result of numerical error accumulation in the evaluation of the convolution integrals. The same excellent agreement with the analytical results is obtained at any location, as shown in [4].

C. EM Field Radiated by an Integrated Antenna in a Layered Configuration

The second experiment concerns the evaluation of the EM-field quantities in the considered layered configuration at $\boldsymbol{x}'_1 = 4\boldsymbol{i}_1 + 1\boldsymbol{i}_3\ (\rm mm)$, that is, close to grazing angles, and at $\boldsymbol{x}'_2 = 4\boldsymbol{i}_1 + 10\boldsymbol{i}_3\ (\rm mm)$, that is, close to broadside. (see Figs. 4). The field quantities are computed by taking the rays up to $n = 4$ (10 rays). The normalization in the plots is similar with that employed in Section IV-B, with $\tau_{\rm a}$ denoting, in this case, the direct ray's arrival time.

Comparing Figs. 3 and 4 illustrates the modifications resulting from the addition of the dielectric layer, the changes being mainly visible in the magnetic behavior. The radiated pulse is still clearly recognizable, which is beneficial for signal transfer applications. The $\boldsymbol{x}' = \boldsymbol{x}'_2$ signatures in Fig. 4 show a lower influence of the rays reflected from the conductive half-space. They are also evidence of the magnetic field's flipping that is characteristic for the near- and intermediate-field regions [34].

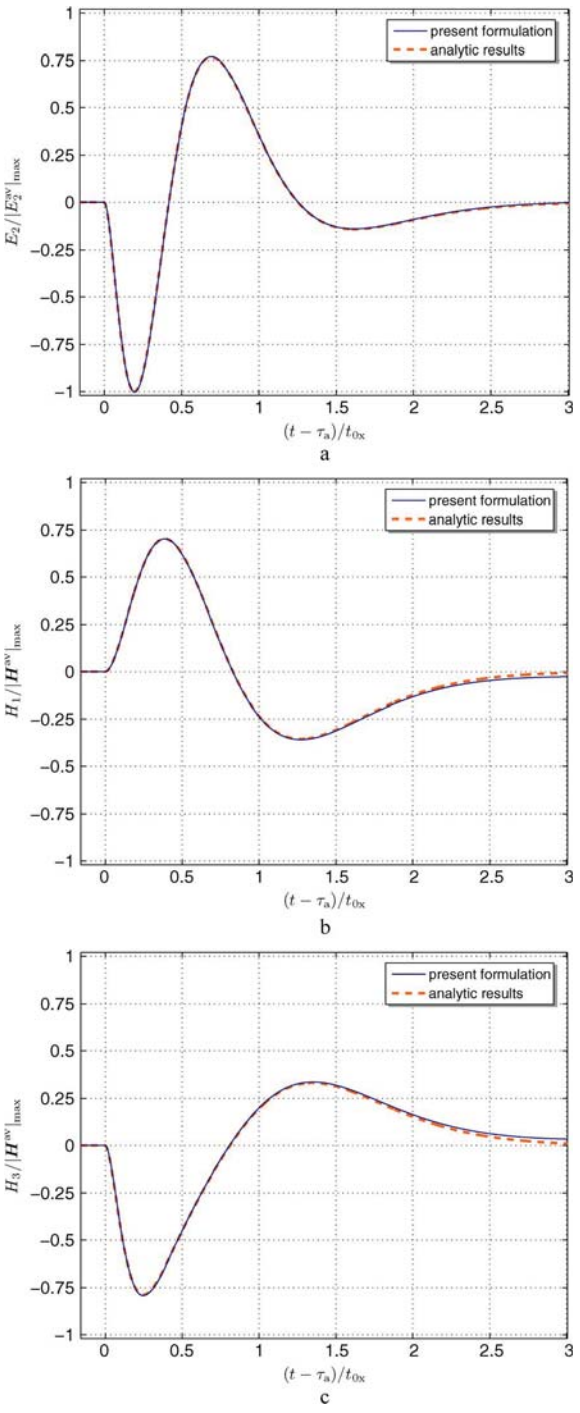

Fig. 3. Comparison between the results determined with the present formulation and the corresponding analytical results at $\boldsymbol{x}' = 4\boldsymbol{i}_1 + 1\boldsymbol{i}_3\ (\rm mm)$. The arrival time is, in this case, $\tau_{\rm a} = |\boldsymbol{x}'|/c_1$. The field quantities are normalized with respect to the analytical values. (a) Normalized E_2, (b) normalized H_1, and (c) normalized H_3.

It is noted that the total computation time amounted in this case to 55 min on an IntelCoreDuo CPU at 3-GHz computer, with 79% of the time being used for calculating the integrals over q and ξ, 19.5% for determining $\mathcal{C}-\mathcal{H}$, and 1.5% for all other tasks. Measures for reducing the computation times are currently explored.

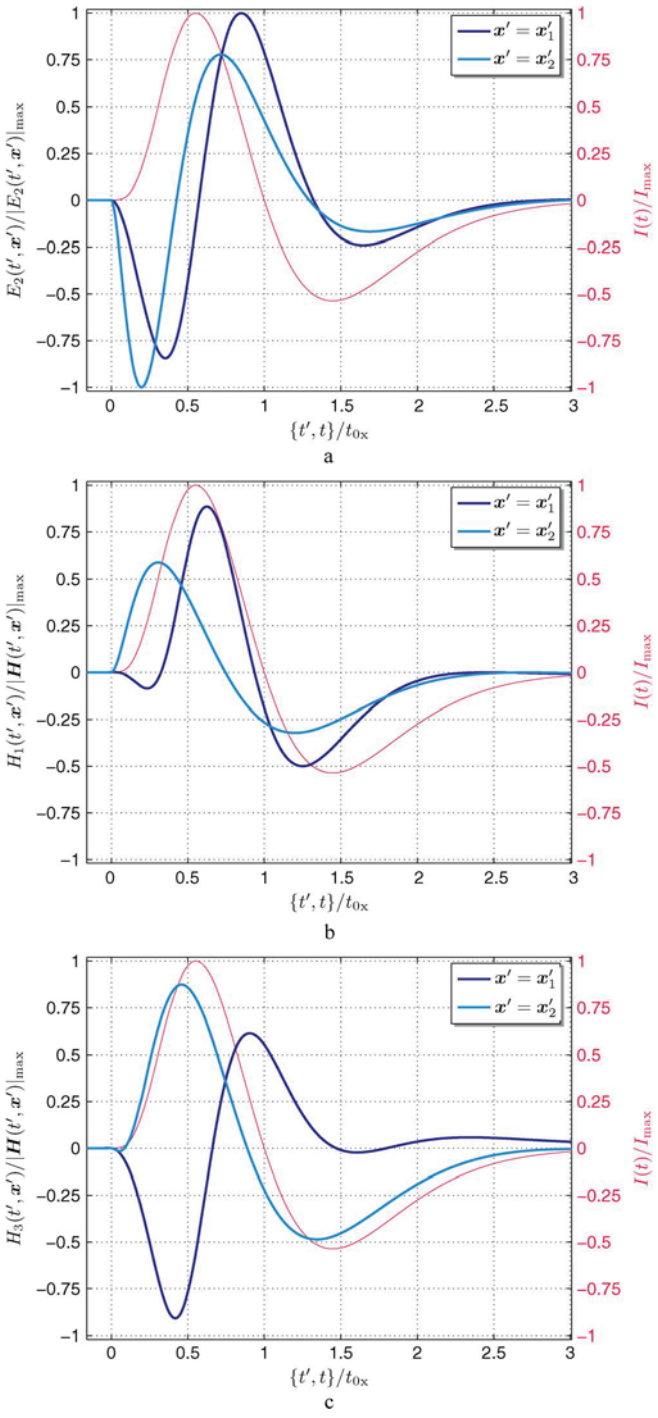

Fig. 4. EM-field quantities at $\boldsymbol{x}'_1 = 4\boldsymbol{i}_1 + 1\boldsymbol{i}_3$ (mm) and $\boldsymbol{x}'_2 = 4\boldsymbol{i}_1 + 10\boldsymbol{i}_3$ (mm), evaluated with eight generalized rays. (a) $E_2(t', \boldsymbol{x}')/|E_2(t', \boldsymbol{x}')|_{\max}$; (b) $H_1(t', \boldsymbol{x}')/|\boldsymbol{H}(t', \boldsymbol{x}')|_{\max}$; (c) $H_3(t', \boldsymbol{x}')/|\boldsymbol{H}(t', \boldsymbol{x}')|_{\max}$. $t' = t - \tau_{\mathrm{a}}$ denotes the arrival time retarded and time coordinate, with τ_{a} being the direct ray's arrival time. The shape of the exciting pulse is provided for comparison.

The presented examples attest the method's ability to provide accurate results with a very high (in fact, arbitrary) time resolution, irrespective of the sampling point's location and devoid of any correlation with spatial parameters, such would be the case with purely numerical techniques. This feature is instrumental for carrying out system performance prediction, especially in the case of pulse shapes with very fast rising and fall off times as the ones employed in this paper.

More numerical examples, not included here for brevity, are available in [27].

D. Computational and Conceptual Advantages of the Proposed Formulation

The results discussed in Sections IV-B and C provide the grounds for comparing the presented method with established, purely computational techniques. Evidently, this method does not offer the same flexibility as general-purpose software packages. Its applicability is restricted to the class of configurations that can be mapped on the one in Fig. 1. However, this limitation is balanced by some categoric advantages:

- it offers arbitrary spatial *and* temporal resolution;
- it allows determining the EM-field quantities at specific locations without the need to examine complete domains;
- it does not suffer from numerical artifacts, most notably from spurious reflections from boundaries and the effect of incongruent electric and magnetic interfaces;
- it offers valuable insight into the modeled phenomena.

The fact that the method allows determining the radiated EM-field quantities at arbitrary locations and with excellent temporal resolution is pivotal for performance prediction and accurate electromagnetic interference or signal integrity estimation in digital signal-transfer systems. Furthermore, this feature represents a cogent argument for using these results as benchmarks for EM computational packages.

V. Conclusion

Pulsed EM-field propagation was examined in configurations that are of relevance for complementary metal–oxide semiconductor integrated antennas. By using the modified Cagniard method, space-time expressions of the EM-field quantities in layered structures with realistic material parameters were obtained. The obtained results were shown to be in excellent agreement with ones following from analytical expressions that are available for free-space propagation. Once the method's accuracy was established, it was employed for analyzing a configuration that is illustrative for the close-range, pulsed EM field, (digital) signal transfer. This formulation has the ability to provide highly accurate results with practically arbitrary temporal resolution, recommending it as an expedient analysis and design instrument.

Appendix

A. Cagniard-DeHoop Contour Features

For being able to infer the Laplace transform by inspection, an opportune parametrization was introduced in Section III-D via (43). This defines the so-called "Cagniard-deHoop" contour $\mathcal{C} - \mathcal{H} = \omega(\xi) \cup \omega^*(\xi)$ (see Fig. 5). Its intersection with the real axis (denoted by "D" in the figure) follows from the expression:

$$\partial_\omega \xi = r - \omega\gamma_1^{-1} Z_1 - \omega\gamma_2^{-1} Z_{\varsigma;2} = 0, \text{ for } \varsigma = \uparrow, \downarrow \qquad (53)$$

for $\mathrm{Im}(\omega) = 0$. Note that γ_1 and γ_2, as given in (34), are also real in this case. Solving (53) gives $\omega = \omega_0$ that, when filled in (43), induces a mapping $\xi = T(q)$. By observing that in the

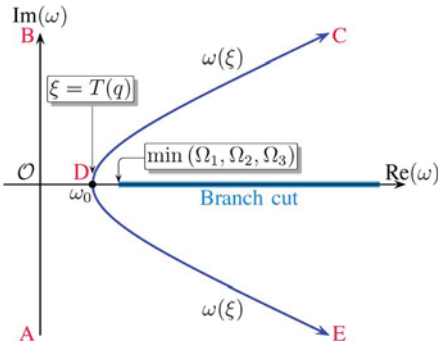

Fig. 5. Cagniard–DeHoop contour ($\mathcal{C}-\mathcal{H}$).

configuration under investigation $c_1 > c_2 > c_3$, (34) implies, upon taking $q = 0$, that $\Omega_1 < \Omega_2 < \Omega_3$. By now invoking Snell's refraction law at $\mathcal{I}_{1,2}$ (see Fig. 1) it follows that [27]:

$$\omega_0 = \Omega_1 \sin(\theta_1) = \Omega_2 \sin(\theta_2) \tag{54}$$

with $0 \leqslant \theta_1 \leqslant \pi/2$ denoting the refraction angle in $\mathcal{D}_1$ and $\theta_2 < \theta_1$ the incidence angle in $\mathcal{D}_2$. It is clear that $\max(\omega_0) = \Omega_1$, corresponding to $\theta_1 = \pi/2$ (grazing angles). Nonetheless, (34) yields in this case $\gamma_1 = 0$ that, in turn, renders (53) singular. This situation is excluded in this paper by always accounting for a nonvanishing vertical shift from $\mathcal{I}_{1,2}$ of the observation points (a choice that is justified by the fact that a receiving antenna cannot be located *at* that interface).

The conditions in (34) require a branch cut in the ω-plane along $\{\omega \in \mathbb{C}; \min(\Omega_1, \Omega_2, \Omega_3) = \Omega_1 \leqslant \mathrm{Re}(\omega); \mathrm{Im}(\omega) = 0\}$. The aforementioned discussion allows concluding that $\mathcal{C} - \mathcal{H}$ never intersects that branch cut.

B. Handling the s-Dependence of $\hat{R}^n_{2,3}(s)$

The Cagniard–DeHoop method is standardly applied to lossless, layered configurations. Nonetheless, the nonzero conductivity in $\mathcal{D}_3$ results in an s-dependence of $\hat{R}_{2,3}$ [see (18), (30) and (31)] that needs to be removed before invoking the Cagniard–DeHoop formalism. The strategy adopted to this end is reminiscent of that in [38], with the conceptual extension of carefully investigating its applicability conditions. For clarity, all manipulations in this Appendix are performed in a complex p-plane, with p and s being identified in the relevant expressions in the main text, as applicable.

To begin with, $\hat{R}^n_{2,3}(p)$ is rewritten as

$$\hat{R}^n_{2,3}(p) = R_{0;n} + \int_{\kappa=0}^{\infty} R_{\mathrm{D};n}(\kappa) \exp(-p\kappa)\mathrm{d}\kappa, \text{ for } n = 0, 1, 2, \ldots \tag{55}$$

in which

$$R_{0;n} = \lim_{|s|\to\infty} \hat{R}^n_{2,3}(p) = \left(\frac{\gamma_2 - \gamma_3}{\gamma_2 + \gamma_3}\right)^n \tag{56}$$

is the instantaneous response of the reflection coefficient (a p-independent quantity) and

$$R_{\mathrm{D};n}(\kappa) = \frac{1}{2\pi\mathrm{i}} \int_{p\in\mathrm{Br}} \hat{R}_{\mathrm{D};n}(p) \exp(p\kappa)\,\mathrm{d}p, \text{ with } \mathrm{Re}(p) > 0 \tag{57}$$

with Br denoting the Bromwich path and $\hat{R}_{\mathrm{D};n}(p) = \hat{R}^n_{2,3}(p) - R_{0;n}$. Note that $\hat{R}_{\mathrm{D};n}(p)$ is constructed such that it satisfies Jordan's lemma in the complex p-plane. To evaluate the integral in (57), the integral path is closed with a semicircle to the *left* of Br, the corresponding integral vanishing in view of Jordan's lemma. Subsequently, (18) is rewritten as

$$\hat{R}_{2,3}(p) = \frac{p\gamma_2 - \gamma_3[p(p+\beta)]^{\frac{1}{2}}}{p\gamma_2 + \gamma_3[p(p+\beta)]^{\frac{1}{2}}}, \text{ with } \mathrm{Re}\left[\left(\gamma_3^2 + p^{-1}\sigma_3\mu_3\right)^{\frac{1}{2}}\right] \geqslant 0 \tag{58}$$

with $\beta = \sigma_3\mu_3\gamma_3^{-2}$, that induces a branch cut interconnecting the branch points $\bar{p}_1 = 0$ and $\bar{p}_2 = -\beta$. By means of Cauchy's theorem, the integral along Br is then equal to the integral along a closed contour enclosing that branch cut. This contour integral is evaluated by a $\{p \mapsto \psi\}$ change of variable according to

$$p = -\beta/2\,[1 - \cos(\psi)], \text{ with } 0 \leqslant \psi < 2\pi \tag{59}$$

that, in turn, implies that

$$\mathrm{d}p = -\beta/2 \sin(\psi)\mathrm{d}\psi \tag{60}$$

$$[p(p+\beta)]^{\frac{1}{2}} = \frac{\mathrm{i}\beta}{2\sin(\psi)}. \tag{61}$$

Using these expressions transforms (57) as

$$R_{\mathrm{D};n}(\kappa) = \frac{\beta\mathrm{i}}{4\pi} \int_{\psi=0}^{2\pi} \left\{\frac{\gamma_2\,[1 - \cos(\psi)] + \mathrm{i}\gamma_3 \sin(\psi)}{\gamma_2\,[1 - \cos(\psi)] - \mathrm{i}\gamma_3 \sin(\psi)}\right\}^n \times \exp\{-\beta/2\,[1 - \cos(\psi)]\,\kappa\} \sin(\psi)\mathrm{d}\psi \tag{62}$$

with the contribution of $R_{0;n}$ to the integral vanishing since

$$\int_{\psi=0}^{2\pi} \exp\{-\beta/2\,[1 - \cos(\psi)]\,\kappa\} \sin(\psi)\mathrm{d}\psi = 0. \tag{63}$$

The expression in (62) lends itself to a straightforward numerical quadrature (e.g., by using standard Matlab functions) and is used in the main text.

It must be noted that changing the integration path in (41) from the imaginary ω-axis to $\mathcal{C} - \mathcal{H}$ has repercussions on the location of the branch point $\bar{p}_2 = -\beta$. As long as $\mathrm{Re}(\omega) = 0$, (14), (32), (33), and (35) ensure that $\gamma_3 \in \mathbb{R}$ and $\gamma_3 > 0$ that, in turn, implies that $\bar{p}_2 \in \mathbb{R}$, with $\bar{p}_2 < 0$. However, for $\omega \in \mathcal{C}-\mathcal{H}$, $\bar{p}_2$ is, in general, complex. Nonetheless, it can be easily shown that

$$|\gamma_3|^2 = \left[q^2 + c_3^2 - \mathrm{Re}(\omega)^2 + \mathrm{Im}(\omega)^2\right]^2 + \mathrm{Re}(\omega)^2\mathrm{Im}(\omega)^2. \tag{64}$$

Since $(q^2 + c_3^2 - \omega_0) > 0$, it is clear that $|\gamma_3|^2$ is always nonzero and, thus, $\mathrm{Re}(\gamma_3^{-2})$ and $\mathrm{Im}(\gamma_3^{-2})$ are finite. Consequently, even

when $\mathrm{Re}(\bar{p}_2) > 0$, its value is finite, and $\mathrm{Re}(p)$ in (55) can be taken large enough for ensuring the absolute convergence of the integral that, in turn, ensures the existence of the relevant Laplace transform.

C. Transformation of the Integrals in the Green's Function

By examining the ray function (41) it can be established that $G^{E}_{k;\varsigma;n}(\omega, q)$ are $O(1)$ and $G^{H}_{k;\varsigma;n}(\omega, q)$ are $O(\omega)$, with O denoting the Landau order symbol [33, p. 1019]. Consequently, $G^{E,H}_{k;\varsigma;n}(\omega, q)$ does not satisfy the conditions required by Jordan's lemma. For handling the integral along the imaginary ω-axis in that equation, use is then made of the artifice $\exp(as) = \partial_s^m \exp(as)/a^m$, with a being an arbitrary parameter, that, for $m = 2$, allows rewriting (41) as

$$\hat{g}^{E,H}_{k;\varsigma;n}(\boldsymbol{x}', s) = \frac{\mathrm{d}^2}{\mathrm{d}s^2}\left(\frac{-1}{8\pi^2}\int_{q=-\infty}^{\infty}\int_{\omega=-\mathrm{i}\infty}^{\mathrm{i}\infty}\int_{\kappa=0}^{\infty}\frac{\mathrm{i}G^{E,H}_{k;\varsigma;n}(\omega, q)}{(\omega r + \gamma_1 Z_1 + \gamma_2 Z_{\varsigma;2} + \kappa)^2} \times \exp\left[-s(\omega r + \gamma_1 Z_1 + \gamma_2 Z_{\varsigma;2} + \kappa)\right]\mathrm{d}\kappa\mathrm{d}\omega\mathrm{d}q\right). \quad (65)$$

This transformation may result in introducing a singularity at $\tau = 0$ [see (44)]. However, apart from the fact that τ is defined such that it never equals zero, it can be shown that the contribution of the residue corresponding to this singularity vanishes (the relevant residue is a polynomial of degree one in s that is then subject to a second-order derivative).

With the new integrand conforming to the conditions required by Jordan's lemma, the relevant integrals on the arcs of radius $\Delta \to \infty$ connecting $\mathrm{B} \leftrightarrow \mathrm{C}$ and $\mathrm{E} \leftrightarrow \mathrm{A}$ in Fig. 5 vanish. Consequently, by invoking Cauchy's theorem, the integral along the imaginary ω-axis can be replaced by an integral along the $\omega(\xi)$ path. Furthermore, a change of variables $\{\omega(\xi), \kappa\} \mapsto \{\xi, \tau\}$ with the Jacobians

$$\partial_\xi \omega = \left(r - \omega\gamma_1^{-1}Z_1 - \omega\gamma_2^{-1}Z_{\varsigma;2}\right)^{-1}, \text{ for } \varsigma = \uparrow, \downarrow \quad (66)$$

$$\partial_\tau \kappa = 1 \quad (67)$$

[see (43) and (44)], and using Schwarz's reflection principle and changing the order of integration transforms (65) into

$$\hat{g}^{E,H}_{k;\varsigma;n}(\boldsymbol{x}', s) = \frac{\mathrm{d}^2}{\mathrm{d}s^2}\left(\frac{1}{4\pi^2}\int_{\tau=\tau_\mathrm{a}}^{\infty}\exp(-s\tau)\mathrm{d}\tau\int_{q=-Q(\tau)}^{Q(\tau)}\int_{\xi=T(q)}^{\tau} \times \mathrm{Im}\left\{\frac{G^{E,H}_{k;\varsigma;n}\left[\omega(\xi), q\right]}{\tau^2\left(r - \omega\gamma_1^{-1}Z_1 - \omega\gamma_2^{-1}Z_{\varsigma;2}\right)}\right\}\mathrm{d}\xi\mathrm{d}q\right). \quad (68)$$

Since all existence conditions of the intervening integrals have now been established, $\mathrm{d}^2/\mathrm{d}s^2$ can commute with the integral. Straightforward algebra then yields

$$\hat{g}^{E,H}_{k;\varsigma;n}(\boldsymbol{x}', s) = \frac{1}{4\pi^2}\int_{\tau=\tau_\mathrm{a}}^{\infty}\exp(-s\tau)\mathrm{d}\tau\int_{q=-Q(\tau)}^{Q(\tau)}\int_{\xi=T(q)}^{\tau} \times \mathrm{Im}\left\{\frac{G^{E,H}_{k;\varsigma;n}\left[\omega(\xi), q\right]}{\left(r - \omega\gamma_1^{-1}Z_1 - \omega\gamma_2^{-1}Z_{\varsigma;2}\right)}\right\}\mathrm{d}\xi\mathrm{d}q \quad (69)$$

and this expression is used in the main text.

Acknowledgment

The authors would like to thank Prof. A. T. de Hoop for the instrumental conceptual clarifications and conducive technical advice that were received throughout the effectuation of the reported research.

References

[1] H.-J. Song and T. Nagatsuma, "Present and future of terahertz communications," *IEEE Trans. THz Sci. Technol.*, vol. 1, no. 1, pp. 256–263, Sep. 2011.

[2] H. Lücken, "Communication and localization in UWB sensor networks. A synergetic approach" PhD dissertation, ETH Zürich, Zürich, Switzerland, 2012. [Online]. Available: http://e-collection.library.ethz.ch/view/eth:6540

[3] I. E. Lager, A. T. de Hoop, and T. Kikkawa, "Pulsed-field wireless interconnects in digital integrated circuits—A time-domain signal transfer and electromagnetic emission analysis," in *Proc. 6th EuCAP*, Prague, Czech Republic, Mar. 2012, pp. 1855–1859.

[4] V. Voogt, I. E. Lager, and B. J. Kooij, "Loop-to-loop pulsed electromagnetic field signal transfer in layered configurations—Application to inter-chip wireless communication," in *Proc. 7th EuCAP*, Gothenburg, Sweden, Apr. 2013, pp. 952–956.

[5] L. Cagniard, *Reflection and Refraction of Progressive Seismic Waves*. New York: McGraw-Hill, 1962, (Translation by E. Flinn, C. H. Dix, of Réflexion et réfraction des ondes séismiques progressives, Paris, Gauthier-Villars, 1939).

[6] A. T. de Hoop, "A modification of Cagniard's method for solving seismic pulse problems," *Appl. Sci. Res., Sect. B*, no. 8, pp. 349–356, May 1960.

[7] A. T. de Hoop and H. J. Frankena, "Radiation of pulses generated by a vertical electric dipole above a plane, non-conducting, earth," *Appl. Sci. Res., Sect. B*, no. 8, pp. 369–377, May 1960.

[8] A. T. de Hoop, M. Štumpf, and I. E. Lager, "Pulsed electromagnetic field radiation from a wide slot antenna with a dielectric layer," *IEEE Trans. Antennas Propag.*, vol. 59, no. 8, pp. 2789–2798, Aug. 2011.

[9] M. Štumpf, A. T. de Hoop, and G. A. E. Vandenbosch, "Generalized ray theory for time-domain electromagnetic fields in horizontally layered media," *IEEE Trans. Antennas Propag.*, vol. 61, no. 5, pp. 2676–2687, May 2013.

[10] W. C. Chew and S.-Y. Chen, "Response of a point source embedded in a layered medium," *IEEE Antennas Wireless Propag. Lett.*, vol. 2, no. 7, pp. 254–258, Aug. 2003.

[11] J. R. Mosig and A. A. Melcón, "Green's functions in lossy layered media: Integration along the imaginary axis and asymptotic behavior," *IEEE Trans. Antennas Propag.*, vol. 51, no. 12, pp. 3200–3208, Dec. 2003.

[12] M.-Y. Xia, C. H. Chan, Y. Xu, and W. Cho Chew, "Time-domain Green's functions for microstrip structures using Cagniard-de Hoop method," *IEEE Trans. Antennas Propag.*, vol. 52, no. 6, pp. 1578–1585, Jun. 2004.

[13] G. W. Hanson, "Dyadic Green's function for a multilayered planar medium—A dyadic eigenfunction approach," *IEEE Trans. Antennas Propag.*, vol. 52, no. 12, pp. 3350–3356, Dec. 2004.

[14] W. C. Chew, J. L. Xiong, and M. A. Saville, "A matrix-friendly formulation of layered medium Green's function," *IEEE Antennas Wireless Propag. Lett.*, vol. 5, no. 1, pp. 490–494, Dec. 2006.

[15] F. Mesa, R. R. Boix, and F. Medina, "Closed-form expressions of multilayered planar Green's functions that account for the continuous spectrum in the far field," *IEEE Trans. Microw. Theory Tech.*, vol. 56, no. 7, pp. 1601–1614, Jul. 2008.
[16] L. Yan and G. W. Hanson, "Wave propagation mechanisms for intra-chip communications," *IEEE Trans. Antennas Propag.*, vol. 57, no. 9, pp. 2715–2724, Sep. 2009.
[17] J. L. Xiong and W. C. Chew, "A newly developed formulation suitable for matrix manipulation of layered medium Green's functions," *IEEE Trans. Antennas Propag.*, vol. 58, no. 3, pp. 868–875, Mar. 2010.
[18] P. R. Atkins and W. C. Chew, "Fast computation of the dyadic Green's function for layered media via interpolation," *IEEE Antennas Wireless Propag. Lett.*, vol. 9, no. 1, pp. 493–496, May 2010.
[19] R. R. Boix, A. L. Fructos, and F. Mesa, "Closed-form uniform asymptotic expansions of Green's functions in layered media," *IEEE Trans. Antennas Propag.*, vol. 58, no. 9, pp. 2934–2945, Sep. 2010.
[20] Y. P. Chen, W. C. Chew, and L. Jiang, "A novel implementation of discrete complex image method for layered medium Green's function," *IEEE Antennas Wireless Propag. Lett.*, vol. 10, pp. 419–422, May 2011.
[21] M. Lucido, "A new high-efficient spectral-domain analysis of single and multiple coupled microstrip lines in planarly layered media," *IEEE Trans. Microw. Theory Tech.*, vol. 60, no. 7, pp. 2025–2034, Jul. 2012.
[22] Y. P. Chen, W. C. Chew, and L. Jiang, "A new Green's function formulation for modeling homogeneous objects in layered medium," *IEEE Trans. Antennas Propag.*, vol. 60, no. 10, pp. 4766–4776, Oct. 2012.
[23] Z. Song, H.-X. Zhou, K.-L. Zheng, J. Hu, W.-D. Li, and W. Hong, "Accurate evaluation of Green's functions for a lossy layered medium by fast extraction of surface- and leaky-wave modes," *IEEE Antennas Propag. Mag.*, vol. 55, no. 1, pp. 92–102, Feb. 2013.
[24] C. Pastore, F. Gianesello, D. Gloria, J. C. Giraudin, O. Noblanc, and P. Benech, "High performance and high current integrated inductors using a double ultra thick copper module in an advanced 65 nm RF CMOS technology," presented at the SiRF 2009, San Diego, CA, USA, Jan. 2009.
[25] A. Babakhani, X. Guan, A. Komijani, A. Natarajan, and A. Hajimiri, "A 77-GHz phased-array transceiver with on-chip antennas in silicon: Receiver and antennas," *IEEE J. Solid-State Circuits*, vol. 41, no. 12, pp. 2795–2806, Dec. 2006.
[26] SiliconFarEast, Properties of SiO_2 and Si_3N_4 at 300 K, 2004. [Online]. Available: http://www.siliconfareast.com/sio2si3n4.htm
[27] V. Voogt, "Loop-to-loop pulsed electromagnetic field signal transfer in layered configurations—Application to inter-chip wireless communication" M.Sc. dissertation, Delft University of Technology, Delft, the Netherlands, 2013. [Online]. Available: http://repository.tudelft.nl/
[28] B. J. Kooij, "Transient electromagnetic field of a vertical magnetic dipole above a plane conducting Earth," *Radio Sci.*, vol. 25, no. 4, pp. 349–356, Jul./Aug. 1990.
[29] W. C. Chew, *Waves and Fields in Inhomogeneous Media*, 2nd ed. Piscataway, NJ, USA: IEEE, 1995.
[30] D. V. Widder, "Necessary and sufficient conditions for the representation of a function as a Laplace," *Trans. Amer. Math. Soc.*, vol. 33, no. 4, pp. 851–892, Oct. 1931.
[31] D. V. Widder, *The Laplace Transform*. Princeton, NJ, USA: Princeton University Press, 1946.
[32] A. T. de Hoop, I. E. Lager, and V. Tomassetti, "The pulsed-field multiport antenna system reciprocity relation—A time-domain approach," *IEEE Trans. Antennas Propag.*, vol. 57, no. 3, pp. 594–605, Mar. 2009.
[33] A. T. de Hoop, *Handbook of Radiation and Scattering of Waves*. London, U.K.: Academic Press, 1995. [Online]. Available: http://www.atdehoop.com
[34] I. E. Lager and A. T. de Hoop, "Loop-to-loop pulsed electromagnetic field wireless signal transfer," in *Proc. 6th EuCAP*, Prague, Czech Republic, Mar. 2012, pp. 786–790.
[35] I. E. Lager, A. T. de Hoop, and T. Kikkawa, "Model pulses for performance prediction of digital microelectronic systems," *IEEE Trans. Compon., Packag., Manuf. Technol.*, vol. 2, no. 11, pp. 1859–1870, Nov. 2012.
[36] P. K. Saha, N. Sasaki, and T. Kikkawa, "A CMOS monocycle pulse generation circuit in a ultra-wideband transmitter for intra/inter chip wireless interconnection," *Jpn. J. Appl. Phys.*, vol. 44, no. 4B, pp. 2104–2108, Apr. 2005.
[37] "IEEE Acoustics, Speech, and Signal Processing Society," in *Programs for Digital Signal Processing*, Digital Signal Processing Committee, Ed. New York: IEEE, 1979.
[38] M. Štumpf and G. A. E. Vandenbosch, "Time-domain behavior of plasmonic half-spaces," *IEEE Photon. J.*, vol. 4, no. 4, pp. 1236–1246, Aug. 2012.

Ioan E. Lager (SM'14) was born in Braşşov, Romania, on September 26, 1962. He received the M.Sc. degree in electrical engineering from the Transilvania University, Braşşov, Romania, in 1987, the Ph.D. degree in electrical engineering from the Delft University of Technology, Delft, the Netherlands, in 1996, and a second Ph.D. degree in electrical engineering from the Transilvania University in 1998.

He successively occupied research and academic positions with the Transilvania University and the Delft University of Technology, where he is currently Associate Professor. In 1997, he was Visiting Scientist with Schlumberger-Doll Research, Ridgefield, CT, USA. He has a special interest in bridging the gap between electromagnetic-field theory and the design, implementation, and physical measurements of wireless systems. His research interests cover computational electromagnetics and antenna engineering, with an emphasis on pulsed-field electromagnetic propagation and nonperiodic (interleaved) array antenna architectures.

Dr. Lager is active in several antenna engineering European networks, primarily in the "VISTA" COST Action.

Vincent Voogt was born in 's-Gravenzande, the Netherlands, in 1990. He received the B.Sc. and M.Sc. degrees in electrical engineering from the Delft University of Technology, Delft, the Netherlands, in 2011 and 2013, respectively.

Bert Jan Kooij was born in Amersfoort, the Netherlands, on February 11, 1959. He received the B.Sc and M.Sc. degrees in electrical engineering, and the Ph.D. degree in technical sciences from Delft University of Technology, Delft, The Netherlands, in 1984, 1986, and 1994, respectively.

Since 1987, he has been a member of the scientific staff of the Electromagnetic Research Group, Delft University of Technology, where he has carried out research and taught classes in the area of electromagnetics, as well as acoustics, wave propagation, and scattering problems. During a three-month period in 1996, he was a Visiting Scientist at Ecole Supérieure d'Electricité (Supelec), Gif sur Yvette, France. He has worked on transient wave propagation problems in the field of elastodynamics and electromagnetics. His current research interests are the computation of inverse wave-field problems employing iterative techniques based on error minimization and space time-domain wave-field modeling.

Since 2010, he has been a member of the Microwave, Sensing, Signals and Systems Group, Delft University of Technology.